Structural steady states and relaxation oscillations in a two-phase fluid under shear flow: Experiments and phenomenological model

L. Courbin*
Centre de Physique Moléculaire Optique et Hertzienne UMR 5798, 351 Cours de la Libération, 33400 Talence, France and Division of Engineering and Applied Sciences,Harvard University, Pierce Hall, Cambridge, Massachusetts 02138, USA

A. Benayad
Centre de Physique Moléculaire Optique et Hertzienne UMR 5798, 351 Cours de la Libération, 33400 Talence, France and LCTPCM UMR 5624, Helioparc Pau Pyrénées, 2 avenue Pierre Angot, 64053 Pau, France

P. Panizza†
Centre de Physique Moléculaire Optique et Hertzienne UMR 5798, 351 Cours de la Libération, 33400 Talence, France
(Received 13 January 2005; published 4 January 2006)

By means of several rheophysics techniques, we report on an extensive study of the couplings between flow and microstructures in a two-phase fluid made of lamellar (L_α) and sponge (L_3) phases. Depending on the nature of the imposed dynamical parameter (stress or shear rate) and on the experimental conditions (brine salinity or temperature), we observe several different structural steady states consisting of either multilamellar droplets (with or without a long range order) or elongated (L_3) phase domains. Two different astonishing phenomena, shear-induced phase inversion and relaxation oscillations, are observed. We show that (i) phase inversion is related to a shear-induced topological change between monodisperse multilamellar droplets and elongated structures and (ii) droplet size relaxation oscillations result from a shear-induced change of the surface tension between both coexisting (L_α) and (L_3) phases. To explain these relaxation oscillations, we present a phenomenological model and compare its numerical predictions to our experimental results.

DOI: 10.1103/PhysRevE.73.011501 PACS number(s): 83.10.Gr, 82.70.−y, 83.60.Rs

I. INTRODUCTION

A common property of complex fluids, such as colloidal suspensions, surfactant and microemulsion solutions, emulsions, foams, or pastes, is the existence of large characteristic dimensions compared to molecular sizes [1]. As a result, these materials exhibit strong couplings between their microstructure and the flow field, leading to unusual nonlinear rheological behavior. One class of couplings between flow and microstructure is the deformation and rupture of droplets occurring when shearing two (or more) immiscible fluids [2]. Indeed, by fragmenting large domains, the flow opposes the thermodynamics driving phase separation and therefore leads to the formation of nonequilibrium steady states in which coarsening is stopped [3–8]. These steady states are separated by out of equilibrium transitions whose nature strongly depends on the dynamic variable which is imposed by the experimenter, namely, either σ, the stress, or $\dot{\gamma}$, the shear rate. In regions where $\delta\sigma/\delta\dot{\gamma}<0$, a mechanical instability [9] occurs leading to either shear bandings [10] or structural bistability [11]. As a result, the measured rheological response of the fluid in these regions respectively exhibits a stress or shear rate plateau or a discontinuity of viscosity. The effects of flow can be summarized by shear diagrams. Such diagrams map the different structural steady states observed under flow as a function of a dynamical variable, the shear rate or the stress and a relevant thermodynamic one, typically, the temperature or a composition parameter. Predicting and understanding such couplings is a real challenge in the physics of out of equilibrium which despite some recent success remains still unsatisfying.

Because energy is constantly brought to the system, richer dynamic behavior such as a nonlinear oscillatory or chaotic response is expected. In the few past years, this question has drawn much attention from both experimentalist and theoretician scientific communities. Temporal fluctuations of the viscosity are witnessed near out of equilibrium transitions for several shear-banding systems such as for instance shear thinning [12] or shear thickening [13] wormlike micellar solutions, lyotropic lamellar (L_α) phases [14], L_α/L_3 phase separating mixtures [15], colloidal suspensions [16], or liquid crystal polymers [17]. The exact origin of these observations is still controversial. Many different scenarios such as mechanic or elastic instabilities [12,18], stick-slips mechanism [17], coupling with shear-induced structures (SISs) [14], or with jamming transitions [16] are invoked, but not clearly proved. On the other hand, models of spatiotemporal rheochaos in shear banding systems with single [19] or multibranched constitutive curves [20] are developed, but lack quantitative comparisons with experimental systems. Shear banding is not a necessary ingredient of complex dynamic behavior. Thus, several spatially homogeneous models [21] predict oscillations or period doubling sequences in systems for which the steady flow curve $\sigma(\dot{\gamma})$ is monotonic. Recently, director chaos in sheared nematic has been predicted and observed without any spatial flow inhomogeneity [22].

*Electronic address: lcourbin@deas.harvard.edu
†Electronic address: p.panizza@cpmoh.u-bordeaux1.fr

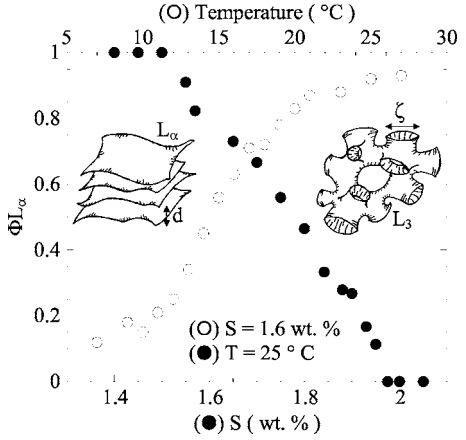

FIG. 1. Phase diagram of the pseudobinary system made of 20 wt % AOT and 80 wt % brine (NaCl in water). Reported on this graph is Φ_{L_α}, the volume fraction of the lamellar phase, as a function of S, the salinity of the brine solvent for $T=25$ °C (●), and as a function of T, the temperature for $S=1.6$ wt % (○). Inset: schematic representations of the microstructures of the L_α phase (smectic distance d) and the L_3 phase (pore size ζ).

In the present paper, we investigate the couplings between flow and structure on a two-phase fluid for which we have previously reported on sustained oscillations at fixed shear rate [23]. This two-phase fluid system consists of coexisting lamellar (L_α) and sponge (L_3) phases. In the first part of the paper, we characterize the effect of flow on this system, as a function of the volume fraction of the L_α phase (experimentally changed by tuning either the temperature or the salinity of the solvent) and of the shear rate (or the stress). Different steady and oscillatory structural states are observed and then mapped on shear diagrams. In the second part of the paper, we present a simple phenomenological model to account for the observed droplet size oscillations and compare its numerical results to our experimental data.

II. EXPERIMENTAL SYSTEM

We work with a pseudobinary mixture of sodium bis(2-ethyl-hexyl) sulfo-succinate (AOT) and brine (sodium chloride). The phase diagram of this system was first reported by Gosh and Miller [24]. It exhibits large domains where membrane phases are thermodynamically stable. For 20 wt % (weight fraction) of AOT, the topology of these phases strongly depends on the brine salinity S and the temperature T. In this water system, the value of the Gaussian curvature $\bar{\kappa}$ strongly depends on the salt content S: $\bar{\kappa}$, which is negative at low S, becomes positive as S increases. On the other hand, the mean curvature modulus κ remains nearly constant ($\kappa \approx 3k_BT$) [25]. As a consequence, for $T=25$ °C, this system presents a lamellar (L_α) phase at low salinities ($S \leqslant 1.5$ wt %) and a sponge L_3 phase for high salinities ($S \geqslant 2.0$ wt %), whereas for intermediate salinities, it exhibits a coexistence between these two phases (see Fig. 1).

In the L_α phase, the membranes are periodically stacked upon one direction whereas in the L_3 phase, they are randomly connected and thus divide space into two equal subvolumes. For $S=1.6$ wt %, coexistence between both L_α and L_3 phases is found for a large range of temperatures (Fig. 1). To study the effect of shear flow on the two phase region of this system, we proceed as indicated in our previous published works [30]. We first stir the mixture to render it macroscopically homogeneous and then introduce it into a transparent Couette cell before shearing it at constant stress or shear rate. This initial stirring of the mixture does not influence the nature of the steady states obtained under controlled shear rate [30]; however, it may affect the kinetics of the formation of such steady states.

III. EXPERIMENTAL TECHNIQUES

To investigate and characterize the effect of flow on the L_α/L_3 two-phase region, we carry on both stress and shear rate controlled experiments. For each experiment, the shear cell is connected to a water bath allowing us to control the sample temperature to within 0.1 °C [stress controlled rheology and small angle light scattering (SALS) measurements] or 0.01 °C [differential interference contrast (DIC) microscopy and small angle neutron scattering (SANS) experiments].

IV. STRESS CONTROLLED EXPERIMENTS

Stress imposed experiments require use of commercial rheometers. To perform *in situ* SALS, we use a homemade transparent Couette cell mounted on a SR5 rheometer (Rheometrics). The inner cylinder (radius $R_i=19$ mm) rotates while the outer one (radius $R_o=19.7$ mm) remains fixed. A circularly polarized He-Ne laser passes through the cell along one of its diameter and probes the sample in the velocity-vorticity ($\mathbf{v},\mathbf{z}$) plane. The scattered pattern which is observed on a screen is digitalized with a charge-coupled device (CCD) video camera coupled to a personal computer. A home made software allows us to determine both isotropic and angular intensity profiles. Because the laser beams crosses the cell twice and therefore the sample, superposition of the scattered light by these two volumes is unavoidable.

The DIC microscopy is performed with a commercial rheoscope (ThermoHaake) using a cone/plate geometry [26]. The values of the radius and the angle of the cell are, respectively, $R=35$ mm and $\beta=1°$. A microscope placed under the plate enables us to observe the texture under flow.

V. SHEAR RATE CONTROLLED EXPERIMENTS

Shear rate applied experiments are performed using Couette cells. Contrary to the Couette geometries used in rheology experiments, the inner cylinders are fixed while the outer ones rotate at a constant velocity ω imposed by the experimenter. With this particular geometry, it is possible to impose the temperature of the stator by connecting the water bath to it, and therefore minimize possible effect of viscous heating [27]. For narrow cell gaps $\dot{\gamma}$, the mean shear rate in the gap is given by $\dot{\gamma}=R_o\omega/(R_o-R_i)$ where R_o and R_i are, respectively, the outer and inner cylinder radii.

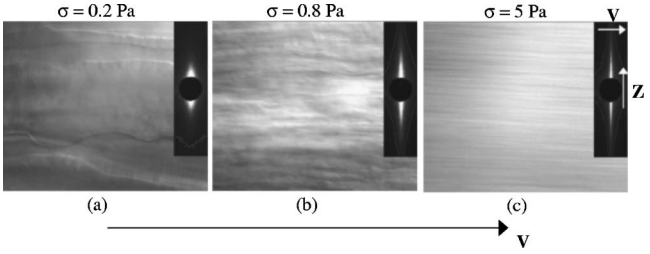

FIG. 2. Steady state texture observed by *in situ* DIC microscopy (magnification ×20) using a cone-plate geometry for $T=14$ °C and different values of the applied stress: $\sigma=$ (a) 0.2, (b) 0.8, and (c) 5 Pa. The size of the images is 230×170 μm^2. Inset: Shown are the SALS patterns, observed in the $(\mathbf{v},\mathbf{z})$ plane using a Couette geometry, for $T=15$ °C and different values of the applied shear rate: $\dot{\gamma}=$ (a) 21, (b) 300, and (c) 1000 s^{-1}.

For SALS experiments, we use a Couette cell made of Plexiglas with $R_i=25$ mm and $R_o=26$ mm. By using two mirrors, an incident circularly polarized laser beam (helium-neon, $\lambda=632.8$ nm in vacuum) parallel to the shear gradient direction ∇v crosses only one of the cell gaps. Contrary to SALS performed at controlled stress, this configuration leads to better results for quantitative analysis since the beam crosses the sample only once. In order to take into account light refraction at the Plexiglas-solution, Plexiglas-water, and Plexiglas-air interfaces optical corrections are computed.

SANS experiments are performed on the PAXY beamline at the Laboratoire Léon Brillouin, (CEA Saclay, France). The BF_3 multidetector, with 128×128 cells of 5×5 mm^2, is positioned at 6 m from the sample. By translating the cell across the incident beam, ($\lambda=0.8$ nm), SANS patterns in the $(\mathbf{v},\mathbf{z})$ and the $(\nabla v,\mathbf{z})$ planes (where ∇v stands for the shear gradient direction) are accessible. The temperature of the water bath connected to our cell was controlled within 0.01 °C.

VI. EXPERIMENTAL RESULTS

A. Temperature diagram

First of all, let us present the different shear-induced structures observed for $S=1.6$ wt % and different temperatures.

1. Low temperature $T\leqslant16$ °C

In this temperature region, a vertical streak along the **z** direction is observed in SALS upon shearing the two phase mixture. This scattering pattern which is similar to that of the so-called *string phase* first observed by Hashimoto and collaborators in polymer mixtures [4] reveals the existence in real space of elongated structures (ESs) along the **v** direction. As the stress is increased, the streak becomes narrower and narrower (see inset in Fig. 2) indicating that the long range orientational order of the structures becomes stronger. Observation in real space shows that the aligned structures along the flow direction (i.e., in the **v** direction) become more and more elongated (see the microscopy images in Fig. 2).

They are not stable at rest since the characteristic streak pattern disappears almost instantaneously if one stops the flow. The texture which is observed between crossed polarizers when the flow is stopped consists of a networks made of focal conics separated by L_3 domains (see the texture in Fig. 3).

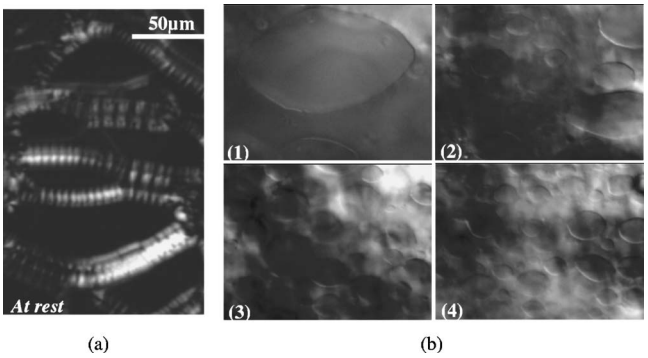

FIG. 3. (a) Texture observed between crossed polarizers at $T=15$ °C (magnification) after stopping the flow (i.e., $\dot{\gamma}=0$ s^{-1}). The value of the preparation shear rate is $\dot{\gamma}=1000$ s^{-1}. (b) Steady textures observed by *in situ* DIC microscopy (magnification ×20) after stopping the flow for different values of the applied stress: $\sigma=$ (1) 0.2, (2) 0.8, (3) 2, and (4) 5 Pa. The value of the temperature is $T=14$ °C.

With DIC microscopy experiments (see Fig. 3) anisotropic droplets are clearly evidenced. Consequently, the droplets are likely made of L_3 phase, and therefore immersed in the lamellar matrix [28]. Since these droplets result from the breakup of the elongated structures, we can conclude that the ESs are made of L_3 phase.

Under flow, the correlation length of the elongated structures along the **z** direction, $\xi_\perp$, can be estimated by analyzing the intensity profiles of the scattered light in this direction using a Lorentzian fit (see Fig. 4 and inset of Fig. 5). As depicted in Fig. 5, $\xi_\perp$ decreases with $\dot{\gamma}$, according to a power law behavior: $\xi_\perp\propto\dot{\gamma}^\alpha$. The value of the exponent $\alpha\approx-1/5$ is very similar to that found for string domains obtained upon shearing two-phase polymer mixtures [29]. Besides, as for string phases, the variation of $\xi_\perp$ with $\dot{\gamma}$ leads to a shear-thinning behavior, characterized by a power law $\eta\propto\dot{\gamma}^{-3/4}$ (see Fig. 6).

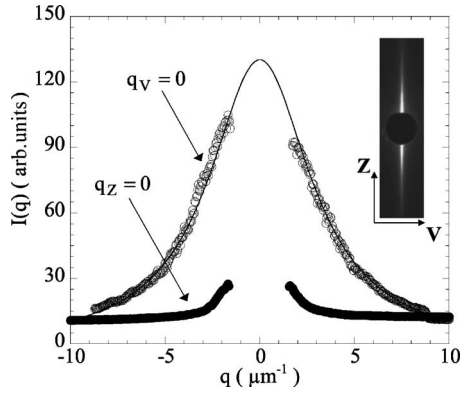

FIG. 4. Variation of the intensity profile along the **z** direction with q_Z for $T=14$ °C and $\dot{\gamma}=1000$ s^{-1}. The equation of the continuous line corresponds to the best Lorentzian fit is $I(q_V=0,q_Z)=2.21+132.41/[1+(0.31q_Z)^2]$ where q_Z is expressed in μm^{-1}. Inset: the corresponding SALS pattern.

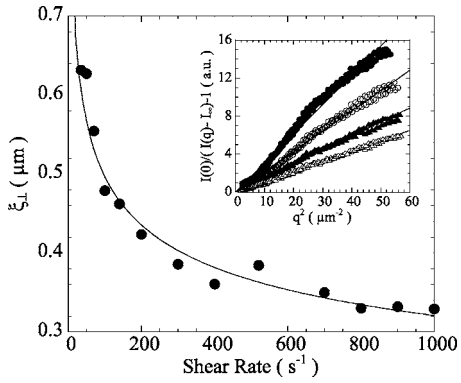

FIG. 5. Variation of the correlation length scale $\xi_\perp$ corresponding to the SIS structures along the **z** direction with $\dot{\gamma}$ for $T=15$ °C. The continuous line represents the best power law fit: $\xi_\perp(\mu\text{m})=1.19\dot{\gamma}^{-0.19}$. Inset: Zimm plots of the intensity of the light scattered along the **z** direction for different values of the shear rate: $\dot{\gamma}=$ (●) 70, (○) 140, (▲) 520, and (△) 1000 s^{-1}. The continuous lines correspond to the best linear fits.

Now, to check whether the L_3 phase transform into the L_α phase under flow or not, we perform SANS experiments (see Fig. 7). This technique also allows us to probe the orientation of the lamellae in both $(\mathbf{v},\mathbf{z})$ and $(\boldsymbol{\nabla}v,\mathbf{z})$ planes (see the SANS spectra in Fig. 7). In the two-phase region, the SANS spectra exhibit a Bragg peak $(q=q_{L_\alpha})$ and bump $(q=q_{L_3})$, respectively, characteristic of the coexisting lamellar and sponge phases. In reciprocal space, the position of the Bragg peak q_{L_α} is related to d, the intermembrane distance according to $d=2\pi/q_{L_\alpha}$ (since the membranes are rigid, $\kappa\approx 3k_BT$ [1]) whereas its intensity is proportional to the volume fraction of lamellar phase. The position in q space of the bump is related to the pore size of the sponge phase according to $\zeta=2\pi/q_{L_3}$ [1] whereas its intensity is proportional to the volume fraction of the sponge phase. As shown in this figure, the intensity of the bump slightly decreases as the shear rate increases indicating that a small fraction of the sponge (less than 10%) phase likely transforms into lamellar phase. As evident in Fig. 7, ζ, the pore size of the L_3 phase, remains unchanged ($\zeta=2\pi/q_{L_3}=16.5$ nm) under flow and most of the L_α phase lamellae exhibit a so-called *a* orientation (i.e., the normal of the layers is directed along **z**). Consequently, under flow, the L_3 domains strongly elongate along the direction **v** whereas the membrane of the lamellar domains orientate perpendicular to the **z** direction (see the SANS patterns in Fig. 7).

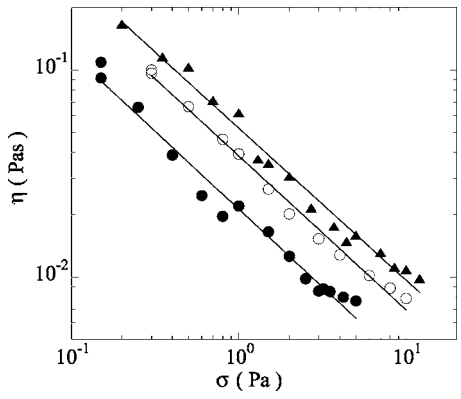

FIG. 6. Steady state viscosity η versus applied stress σ for $T=15$, 17, and 17.6 °C. The equations of the continuous lines which correspond to the best power law fits are, respectively, η (Pa s) $=0.021\sigma^{-0.75}$ (●), (○) $0.038\sigma^{-0.74}$, and (▲) $0.052\sigma^{-0.73}$ where the stress is given in Pa.

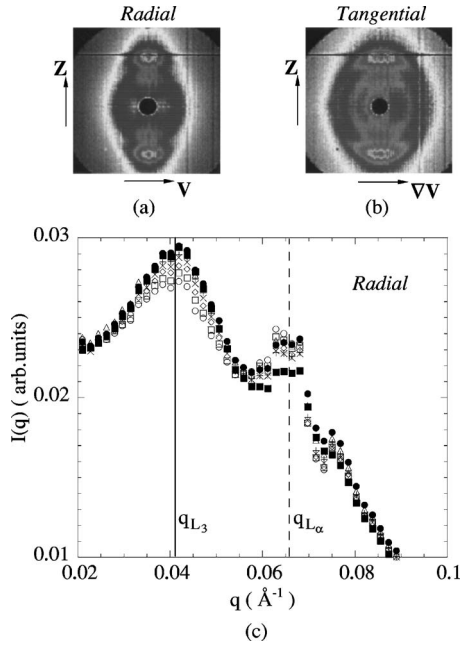

FIG. 7. SANS patterns observed in (a) $(\mathbf{v},\mathbf{z})$ and (b) $(\boldsymbol{\nabla}v,\mathbf{z})$ planes for $\dot{\gamma}=7$ s^{-1}. (c) Shown are the radial isotropic intensity profiles. The different values of applied shear rates are, respectively, $\dot{\gamma}=7$ (■), 20 (●), 50 (△), 75 (+), 100 (×), 150 (◇), 200 (□), and 250 s^{-1} (○). The values of ζ, the phase L_3 pore size, and d, the L_α phase smectic distance, are, respectively, 15.3 and 9.5 nm. The system consists of 20 wt % AOT and 80 wt % brine solution ($S=1.38$ wt %). Replacing water by deuterated water shifts the phase diagram to lower salinities: the volume fraction of lamellar phase is $\Phi_{L_\alpha}\approx 0.35$ and the temperature is fixed at $T=15$ °C.

2. High temperature $T\geqslant 20$ °C

To investigate shear-induced structural changes occurring at higher temperatures, (i.e., for larger values of Φ_{L_α}), we perform a temperature change by rapidly switching the connection between our Couette cell and the water bath set at the temperature $T=T_i$ to another water bath set at $T=T_f$. Figure 8 shows the variation of the viscosity during such a change in temperature. As revealed on this graph, the viscosity strongly depends on temperature. *In situ* SALS experiments prove that this strong increase of the viscosity is related to important structural changes in the mixture. As the temperature increases, the light scattering pattern transforms from the initial vertical streak observed for low temperatures to a well defined scattering ring. Its radius evolves continuously until it reaches its steady state value. In what follows, let us name q_B the position in reciprocal space of this ring. This narrow ring proves the existence in the solution of a unique characteristic length $L=2\pi/q_B$ of the order of a few micrometers. If

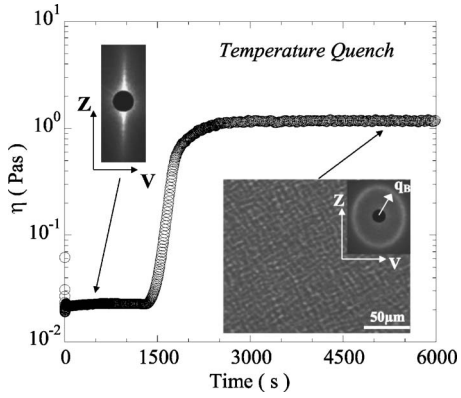

FIG. 8. Temporal variation of the viscosity measured for $\sigma=1.3$ Pa during a temperature quench from $T_i=17$ °C ($t=0$ s) to $T_f=27$ °C ($t=6000$ s). The temperature change is performed at $t=1000$ s. The value of the viscosity which does not vary after $t=6000$ s corresponds therefore to the steady state value for $T=T_f=27$ °C and $\sigma=1.3$ Pa. Insets: observed SALS patterns for $t=0$ and 6000 s, and the final texture observed between crossed polarizers observed for $t=6000$ s (magnification ×10).

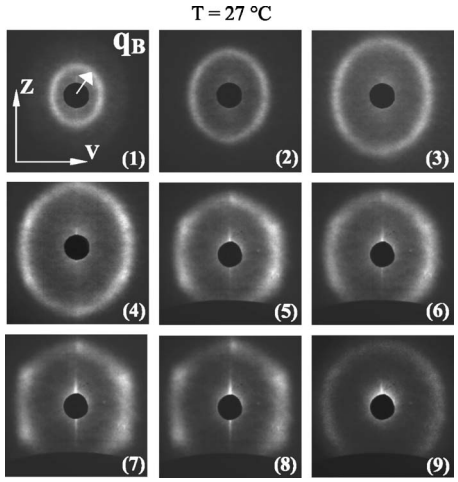

FIG. 9. Evolution of the steady state SALS patterns with $\dot{\gamma}$ for $T=27$ °C. The different values of the applied shear rate are $\dot{\gamma}=$ (1) 25, (2) 35, (3) 50, (4) 70, (5) 200, (6) 300, (7) 400, and (8) 500 s^{-1}, and (9) SALS pattern observed one second after stopping the flow. The value of the preparation shear rate is $\dot{\gamma}=500$ s^{-1}.

the flow is stopped, the ring remains indicating that the isotropic shear-induced texture obtained at high temperature is metastable contrary to the elongated one, found at low temperature. Depending on the values of T_f and $\dot{\gamma}$, it can even persist for a few hours. Using this property, the sample can then be removed from the Couette cell and placed between glass slides for microscopic observations. Note that the size of the scattering ring observed after removal of the sample from the shear cell and transfer between two glass slides does not change, indicating that this process does not affect the structure of our sample. The texture (see inset of Fig. 8) we then observe is characteristic of a glassy assembly made of closed compact monodisperse multilamellar droplets (state *I*), likely separated by L_3 phase films [30].

Assuming that the entire lamellar phase is converted into droplets (a reasonable assumption in view of our microscopic observations), the volume fraction of these droplets therefore corresponds to that of the lamellar phase in the mixture ($\Phi_{L_\alpha}\approx 0.9$ at $T=27$ °C) [30]. The droplets are well beyond close packing and consequently must be polyhedral. The isotropy of the SALS pattern indicates that these droplets are disorderly packed, the characteristic size L corresponding to the distance between two nearest neighbors [30] (Fig. 9). Under the assumption that the entire lamellar phase is converted into droplets, the volume fraction of L_α phase, Φ_{L_α}, is given by $\Phi_{L_\alpha}\approx(R/L)^3$, where L corresponds to the characteristic distance between the droplets [30]. As a consequence, the evolution with the shear rate of the mean droplet size R is identical to that of L. The radius of the ring first increases with shear rate, indicating that in real space the size of the closed compact droplet decreases (Fig. 9). Then, after a critical shear rate, six fuzzy Bragg peaks suddenly emerge on the same ring proving that the droplets now form a colloidal crystal exhibiting a sixfold symmetry in the $(\mathbf{v},\mathbf{z})$ plane (state II). In this region, when the flow is stopped, the long range order is lost since the six peaks fade away and the SALS pattern relaxes to a ring (see SALS pattern 9 in Fig. 9).

At higher shear rates, a vertical streak superposes to the six peaks. Such a superposition proves that when the shear rate is imposed, the transition between regions II (colloidal crystal) and III (elongated structures) occurs via a coexistence region between both structures. In other words, when the value of shear rate is increased, the formation of III occurs through a nucleation and growth process. Optical observations reveal no macroscopic horizontal bands in the Couette cell, and the SALS pattern (six Bragg peaks + a vertical streak) remains unchanged upon vertical translation of the laser beam. In the coexistence region, the bands are therefore set in the gap cell. If one refers to Olmsted's classification [31], the transition II-III is therefore characteristic of an "A-1 common stress phase separation." Note that the nature of this transition drastically differs from that occurring between multilamellar droplets and ribbons in the sodium dodecyl sulfate–water-octanol system [6]. Now, if the stress is imposed, three steady regions can be clearly distinguished by SALS. At low stresses (region I), the solution is quasi-Newtonian and presents in SALS a scattering ring (see Fig. 10).

From q_B, the position of the ring in Fourier space, the size of the closed compact droplets can be estimated (Fig. 10). As expected from Taylor's droplets, it varies as the inverse of σ. In this regime, the droplet size then results from a mechanical balance between capillary and viscous stresses [30]. In the absence of small angle x ray scattering (SAXS) or SANS data in this region we have no proofs of the existence of remaining sponge phase between multilamellar droplets. Therefore, we cannot rule out the possibility that some of the sponge phase may have shear-induced transformed into another lamellar phase L_α^*, different from the L_α phase. However, in this case, invoking the surface tension between the L_α droplets and the phase lying outside to explain the variation of the droplet size with stress (or shear rate), is still correct. For larger stresses (region II), the solution becomes strongly shear thinning and the steady state viscosity varies

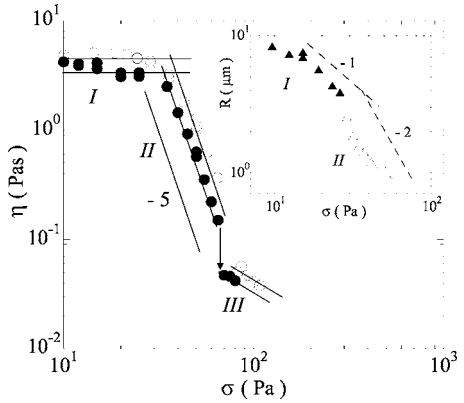

FIG. 10. Shown are log-log plots of the steady state viscosity and of the characteristic size deduced from SALS measurements (inset) versus stress. The different symbols correspond to different values of the temperature: $T=$ (●) 23, (○) 30, and (△, ▲) 27 °C. The continuous and dashed lines are only eye guides. Depending on experimental conditions (used shear cell, distance from the CCD video camera to the screen), the mean droplet size is measured to within 0.15 μm.

accordingly to $\eta \propto \sigma^{-5}$ (i.e., as $\dot{\gamma}^{-0.85}$). In this crystallized region (II), the variation of q_B with σ shows that the droplet size scales differently. Now, when the value of the applied stress is further increased, the Bragg peaks suddenly disappear and a very intense narrow vertical streak along the **z** direction can be witnessed (region III). In this region, the long range ordered multilamellar droplets therefore become unstable and break to form elongated structures along the flow direction. In stress controlled experiments, the transition between regions II and III occurs though a discontinuous jump in the viscosity. The nature of this shear-induced transition strongly depends on the imposed dynamic variable (stress or shear rate). Thus, if one imposes the shear rate, the SALS pattern we observe corresponds to the superposition of the vertical streak and the six Bragg peaks. Finally, let us point out that this transition is related to a *shear-induced phase inversion phenomenon*. At low shear rates, the multilamellar droplets are immersed in the L_3 phase whereas the ESs prepared at high shear rates relaxes when the flow is stopped into L_3 droplets embedded in the L_α matrix similarly to what is observed in (Fig. 3).

3. Intermediate temperature $17 \leqslant T \leqslant 20$ °C

Figure 11 shows the variation of the steady state viscosity with applied stress for intermediate temperatures. Two branches separated by a hysteresis loop are clearly noticeable. At low stresses, the mixture presents a Newtonian behavior characterized in SALS by a narrow scattering ring found at $q=q_B$. Under polarized microscope the texture corresponds to a glassy assembly made of monodisperse multilamellar droplets similar to region I at higher temperature [30].

At high stresses, the solution becomes shear thinning and exhibits in SALS a strong narrow streak along the **z** direction. For intermediate stresses, the steady state viscosity can take two very different values. This results from a structural

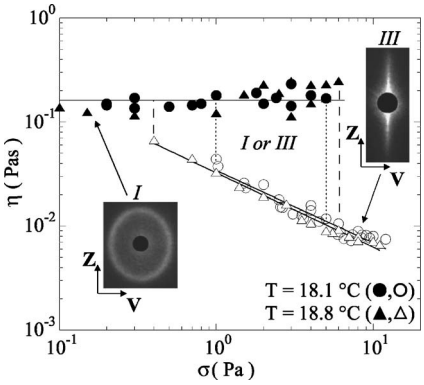

FIG. 11. Log-log plots of the steady state viscosity η versus applied stress σ for $T=18.1$ (●, ○) and 18.8 °C (▲, △). The best power law fits give for the lower viscosity branches η (Pa s)= (○) $0.034\sigma^{-0.69}$ and (△) $0.032\sigma^{-0.71}$. Inset: shown are the two characteristic SALS patterns observed for these two branches.

bistability between a viscous glassy assembly made of monodisperse droplets (region I) and a very low viscous state, consisting of elongated structures (region III).

4. Shear diagram

We have shown the existence of three steady states separated by dynamic transitions. Two of these states are made of droplets, and one of them consists of elongated structures. The regions of stability of these structural states can be summarized by a shear diagram which maps the different observed structural states as a function of stress and temperature (see Fig. 12).

B. Salinity diagram

1. Experiments

As shown in Fig. 1, the fraction of L_α phase in the two-phase region of our system can also be changed by tuning the brine salinity. To check whether or not the shear-induced structural changes previously observed are mainly dependent on the respective volume fraction of the two coexisting phases, we study the influence on salinity at a fixed temperature. In order to do so, we work at $T=25$ °C, with solutions

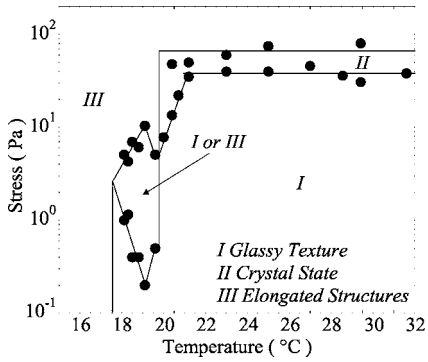

FIG. 12. Different structural steady states observed as a function of stress and temperature. The brine salinity is $S=1.6$ wt %.

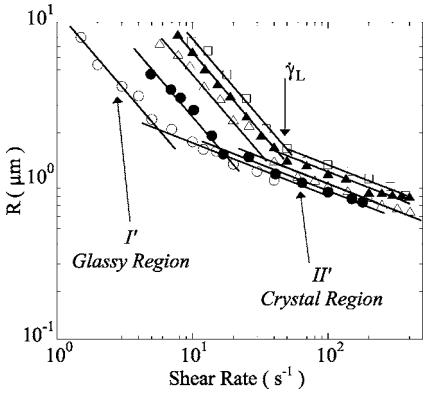

FIG. 13. Variation of R deduced from SALS experiments, with $\dot{\gamma}$ for different values of the brine salinity and $T=25$ °C. The different symbols stand for the different values of S:S=(○)1.51, (●) 1.55, (△) 1.6, (▲) 1.63, and (□) 1.65 wt %. Solid lines correspond to the best power law fits, respectively, for steady states I′ and II′: $R \propto \dot{\gamma}^{-1}$ and $R \propto \dot{\gamma}^{-1/3}$. The mean droplet size is measured to within 0.15 μm.

made of 20 wt % AOT and 80 wt % brine of different salinities. For low salinities ($S \leqslant 1.67$ wt%), we have shown in one of our previous papers, that two distinct structural steady states can be identified as a function of shear rate [30] (Fig. 13).

For low shear rate values, the solutions are Newtonian and present in SALS a scattering ring (region I′). The texture, similar to that of region I, previously described, consists of a glassy assembly made of multilamellar droplets immersed in the L_3 phase. The size of the droplets which decreases when the shear rate increases varies accordingly to $1/\dot{\gamma}$ (see Fig. 13). As previously shown [30], such a scaling law results from a mechanical balance between capillary and viscous force. Above a critical shear rate $\dot{\gamma}_L$, as revealed by the emergence of six scattering peaks in SALS experiments, the droplets organize on a sixfold colloidal crystal in the $(\mathbf{v},\mathbf{z})$ plane (region II′). In this region, the distance between droplets decreases more slowly with $\dot{\gamma}$ since it varies as $\dot{\gamma}^{-1/3}$

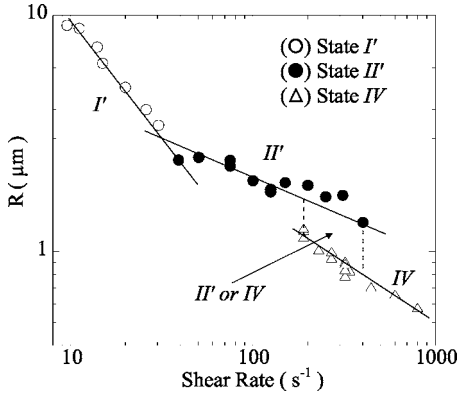

FIG. 14. Shown is R, deduced from SALS measurements as a function of $\dot{\gamma}$ for $T=25$ °C and $S=1.68$ wt %. For each state, the solid line is a guide for the eyes. The value of the slope of the line is, respectively, −1 (state I′), −1/3 (state II′), and −1/2 (state IV). The mean droplet size is measured to within 0.15 μm.

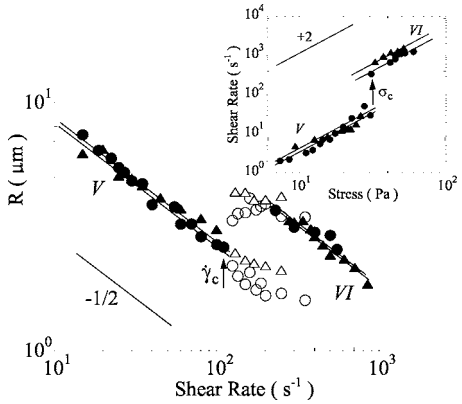

FIG. 15. Shown is R, deduced from SALS measurements as a function of $\dot{\gamma}$ for $T=25$ °C. Inset: Shown is the steady state shear rate versus applied stress. Circles and triangles correspond, respectively, to $S=1.7$ and 1.715 wt %. Closed symbols (●, ▲) represent steady states and open (○, △) symbols stand for the minima and maxima of the size during oscillations. The mean droplet size is measured to within 0.15 μm.

[30]. The two steady states I′ and II′ are indeed identical to the states I and II previously obtained in the study performed as a function of the temperature.

For a slightly different salinity $S=1.68$ wt %, the response of our two phase fluid under flow becomes more complex since a third structural steady state (state IV, see Fig. 14) can now be witnessed at high shear rates.

As shown by SALS experiments, this new steady state is also a colloidal crystal exhibiting a sixfold symmetry in the $(\mathbf{v},\mathbf{z})$ plane. Yet, it can easily be distinguished from the crys-

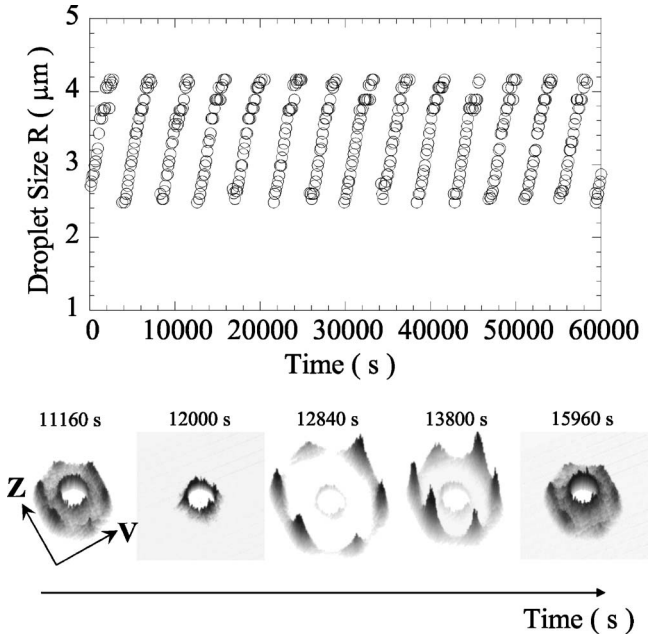

FIG. 16. Temporal variation of the size R, deduced from SALS measurements for $\dot{\gamma}=130$ s^{-1}, $T=25$ °C, and $S=1.715$ wt %. Shown is a 3D representation of the temporal evolution of the scattering pattern in the $(\mathbf{v},\mathbf{z})$ plane. The mean droplet size is measured to within 0.15 μm.

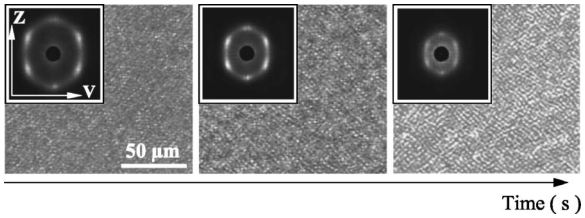

FIG. 17. Temporal evolution of the texture observed between crossed polarizers (magnification ×10) during the continuous growth of the size R for different times. The values of the applied shear rate and of the salt content are, respectively, $\dot{\gamma}=150\ s^{-1}$ and $S=1.715$ wt %.

tal structure observed at lower shear rates (region II′), since first the droplet size scales differently with shear rate ($R \propto \dot{\gamma}^{-1/2}$) and second, it varies discontinuously at the transition II′-IV.

Now, if the salinity is slightly increased ($1.69 \leqslant S \leqslant 1.72$ wt %), an extraordinary phenomenon [23] takes place for shear rate controlled experiments. Two different steady states (states V and VI) are observed at low and high shear rates (see Fig. 15), both structures being colloidal crystals made of multilamellar droplets with a sixfold symmetry in the $(\mathbf{v},\mathbf{z})$ plane. Although these two colloidal crystals exhibit the same symmetry and similar variations of the droplet size with $\dot{\gamma}$ ($R \propto \dot{\gamma}^{-1/2}$), they can however be easily distinguished since the prefactor of R versus $\gamma^{-1/2}$) varies discontinuously at the transition (see Fig. 15).

However, for intermediate values of the shear rates, an unexpected phenomenon is witnessed since the droplet size becomes a periodical function of time [23]. Figure 16 shows the temporal variations of the scattering pattern observed during such an oscillatory regime.

First, the radius of the scattering ring decreases very slowly and continuously until it reaches a minimum size. During this slow process, microscopic observations reveal that the texture remains homogeneous in the whole cell (see Fig. 17). Then, the contrast is suddenly lost and one witnesses the emergence of a scattering ring at a much larger wave vector. During this fast regime (a few seconds long), the solution presents an horizontal interface in the Couette cell and becomes turbid (Fig. 18).

These reproducible oscillations occur above a well-defined critical shear rate $\dot{\gamma}_c$ (see Fig. 15). They do not depend on the flow history of the sample but only on the value of the applied shear rate. We have observed them for different values of the cell gap and of the stator radius. However, in terms of thermodynamic parameters, such as the temperature and salinity, this oscillation phenomenon only seems to occur in a very narrow range (see in Fig. 19 the evolution of the droplet size R as a function of the temperature).

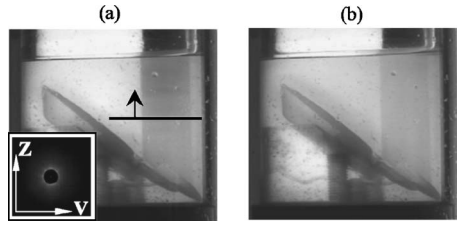

FIG. 18. Visualization of the turbidity enhancement observed during the fragmentation of the droplets (oscillatory regime). Inset: shown is the corresponding SALS pattern.

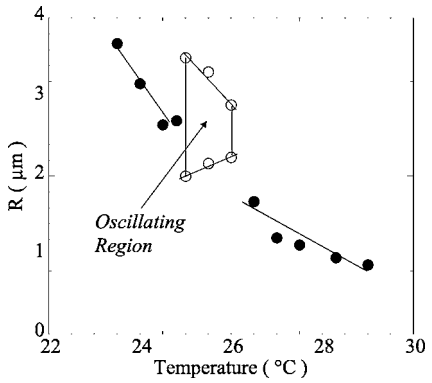

FIG. 19. Variations of the droplet size R as a function of temperature for $\dot{\gamma}=190\ s^{-1}$ and $S=1.69$ wt %. The different symbols respectively stand for steady states (●) and oscillatory regimes (○). In the oscillatory regimes are reported the maximum and minimum size. For $T<23.4$ °C, the solution becomes turbid and the contrast too weak to make a study by SALS possible. The mean droplet size is measured to within 0.15 μm.

Solutions with higher salinities (typically $S>1.72$ wt %) have not been studied because of their very low contrast in SALS which make their study difficult by this technique. The ensemble of our results can be summarized in the shear diagram depicted in the $(S,\dot{\gamma})$ plane (see Fig. 20). As shown on this diagram, at 25 °C the droplet size oscillations are only observed in a very narrow region.

Now, if we impose the stress instead of the shear rate, (these experiments are performed with an SR5 rheometer, using a homemade Couette geometry), both steady state colloidal structures are still observed. Yet the transition between these two colloidal structures occurs at a well-defined critical stress σ_c, through a discontinuous decrease of the viscosity and a discontinuous increase of the droplet size R (see inset in Fig. 15 and Fig. 21).

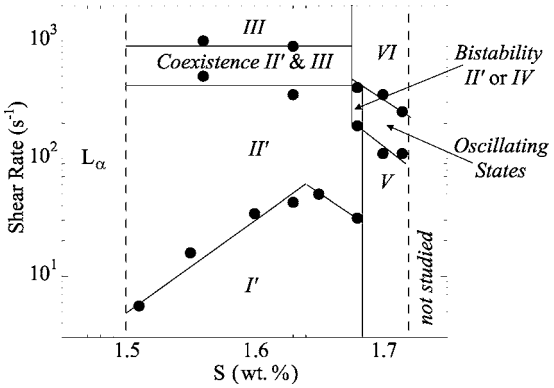

FIG. 20. Out of equilibrium diagram mapping the different steady and oscillatory states observed in the L_α-L_3 two-phase region as a function of S, the salinity of the brine, and $\dot{\gamma}$. Are represented only the salinities which have been studied by SALS.

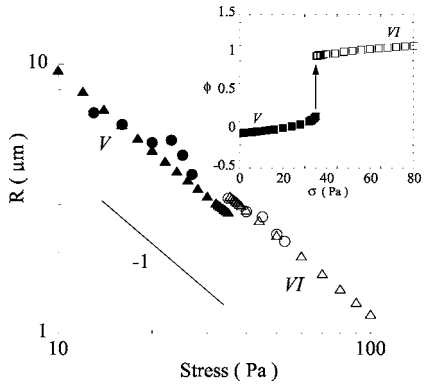

FIG. 21. Variations of both the experimental (●, ○) and the numerical (▲, △) steady droplet size R as a function of the applied stress. Inset: shown is the evolution of the order parameter ϕ (■, □) versus σ. The different symbols respectively stand for state V (●, ▲, ■) and state VI (○, △, □). The solid line is a guide for the eyes and has a slope −1. The values of the numerical parameters and of the salinity are, respectively, $k=5$, $\alpha=0.5$, $\tau_2=65$ s, and $S=1.715$ wt %. The mean droplet size is measured to within 0.15 μm.

In contrast to shear rate controlled experiments, no droplets oscillations are observed for intermediate values of the stress. As previously noted for shear rate controlled experiments, the variation of the droplet size with stress is similar for both steady state structures. The scaling laws we establish ($R \propto \sigma^{-1}$) strongly suggests that the droplet size results in both states from a mechanical balance between capillary and viscous forces (Fig. 21) [3]. Recall that within this picture, the droplet size is expected to vary according to $R \propto \chi/\sigma$ where χ represents the surface tension between both L_α and L_3 phases. Consequently the discontinuous increase of R, experimentally observed at the transition V-VI (see Fig. 15) is likely associated with a discontinuous variation of χ. Following this idea, linear fits of R versus σ^{-1} lead to $\chi_V \approx 9.5 \times 10^{-5}$ N m^{-1} for state V and $\chi_{VI} \approx 11.5 \times 10^{-5}$ N m^{-1} for state VI, two values compatible with results expected from a dimensional analysis [23].

What can be the microscopic origin of such a change in surface tension under flow? For two reasons, we tend to believe that a discontinuity of χ may be triggered by a compression of multilamellar droplets (yielding release of solvent outside). First, such a solvent release has been already observed in another system where the droplets present also a long-range order under flow [32] and a solid-solid transition is witnessed. In this system, both variations of the droplet size and viscosity at the transition are similar to what we observe in our system. Second, a recent study performed in the same pseudobinary AOT-brine system but at a different salinity has proven a fragmentation process of the droplets under flow requiring no transient elongation and triggered by a water release [33]. However preliminary SAXS experiments performed at ESRF (Grenoble, France) do not permit a conclusion yet.

These considerations now raise another important question: what is the feedback mechanism at the origin of droplet size oscillations? We will try to answer this question in the next section of our paper.

2. Droplet size oscillations, discussion, and model

a. Toward a phenomenological description. Let us first try to qualitatively understand the feedback mechanism responsible of the droplet size oscillations. As previously argued, for two reasons, we tend to believe that a discontinuity of the surface tension may result from a compression (when the pressure of the droplets overcomes a critical stress σ_c) of the multilamellar droplets yielding release of solvent outside. Let us consider our system to be on the steady state branch V. If the value of the applied shear rate is slightly increased, the Laplace pressure of the droplets given by $P \approx \chi_V/R$ (where χ_V is the surface tension between L_α and L_3 phases), increases since the droplet size decreases. Thus, sufficiently close to the transition V-VI, it may overcome the value of the critical stress above which the droplets compress by releasing water outside. Following this scenario, the water release induces composition changes of both coexisting L_α and L_3 phases since the intermembrane distance of the L_α phase decreases, whereas that of the L_3 increases. Consequently, the value of the surface tension between both phases is no longer the equilibrium one, but slightly increases and becomes χ_{VI}. As a result, the mean droplet size must increase in order to reach its new mechanical balance between viscous and capillary stresses. When the droplet size increases, the corresponding Laplace pressure decreases and therefore may become smaller than σ_c. If that is the case, water is reintegrated within the droplets and the scenario may start over leading to sustained droplet size oscillations. Because permeation of water through membranes is a very slow process, such a scenario may explain why the period of the oscillations is indeed so large. Such a feedback mechanism involves two distinct but coupled processes, namely, the dynamics of the droplet size and that of the transfer of water. Thus, two differential equations are necessary to model this phenomenon. The first equation must describe the mechanical dynamics of the droplet size whereas the second one must concern the osmotic release of water by the droplets. The simplest way to describe the mechanical evolution of the droplet size $R(t)$ is to consider a first order kinetic process. Now, if one recalls that the droplet size results for both steady state branches from a mechanical balance between viscous and capillary stresses, a good candidate for the first equation is

$$\dot{R} = -\frac{1}{\tau_1}\left(R - \frac{\chi(\phi)}{\sigma}\right), \tag{1}$$

where $\chi(\phi)$ is the surface tension under flow between both coexisting and viscous stress; ϕ being a variable characterizing the compression of the droplets. For simplicity's sake, we consider that $\phi \approx 0$ for uncompressed droplets and $\phi \approx 1$ for compressed ones. On the other hand, σ and τ_1 represent, respectively, the viscous stress and the characteristic time to reach mechanical equilibrium. Note that for shear rate controlled experiments, σ corresponds to the steady state measured stress, namely, $\sigma = \eta(\phi, \dot{\gamma})\dot{\gamma}$ where $\eta(\phi, \dot{\gamma})$ corresponds to the viscosity of the system. To de-

TABLE I. Report of the parameters contained in the model. Six of the nine parameters are obtained from experimental techniques.

Parameter	Value	Method
χ_V	9.5×10^{-5} N m^{-1}	SALS+rheology
χ_{VI}	11.5×10^{-5} N m^{-1}	SALS+rheology
A_V	5.18 Pa s^2	Rheology
A_{VI}	1.73 Pa s^2	Rheology
σ_c	30 Pa	Rheology
τ_1	650 s	SALS (see Ref. [23])
τ_2	Unknown	
k	Unknown	
α	Unknown	

scribe the nonlinear release of water by the droplets, we must now find a differential equation governing the dynamics of ϕ, the order parameter. This equation must describe the dynamics of a first order phase transition between region V (uncompressed state, $\phi\approx0$) and region VI (compressed state, $\phi\approx1$) triggered by the Laplace pressure of the droplets. Therefore, we consider the following differential equation:

$$\dot{\phi}=-\frac{1}{\tau_2}\left(-\frac{\chi(\phi)/R-\sigma_c}{\sigma_c}-\alpha(2\phi-1)+(2\phi-1)^k\right), \quad (2)$$

where τ_2 and σ_c are, respectively, a characteristic time associated with the slow permeation of water through the membranes and the critical stress above which the droplets compress. k and α are numerical constants which, respectively, monitor the stiffness of the transition with respect to shear rate and the amplitude of the size change when the droplet size oscillates. Solving this set of two equations, requires us to know the functions $\chi(\phi)$ and $\eta(\phi,\dot{\gamma})$. However, rheological measurements simplify this problem since they reveal that $\eta(\phi,\dot{\gamma})=A(\phi)\dot{\gamma}^{-1/2}$. Therefore, only two functions $\chi(\phi)$ and $A(\phi)$ have to be inserted in our phenomenological model. However, we know a few things about them. First of all, their values can be experimentally found for $\phi\approx0$ (region V) and $\phi\approx1$ (region VI). Moreover, these two functions are likely monotonic. That is why to limit the number of free parameters in our model, in a first approximation, we assume that these two functions are simply linear interpolations, namely,

$$\chi(\phi)=\chi_V(1-\phi)+\chi_{VI}\phi \quad (3)$$

and

$$A(\phi)=A_V(1-\phi)+A_{VI}\phi. \quad (4)$$

We believe that the physics aspect of the model is not contained in the exact mathematical form of these two functions, provided that they are monotonic. Although, our simple model contains nine parameters, six of them can be directly determined by experimental methods (see the Table I). Consequently only three parameters remain unknown, namely, k, α, and τ_2.

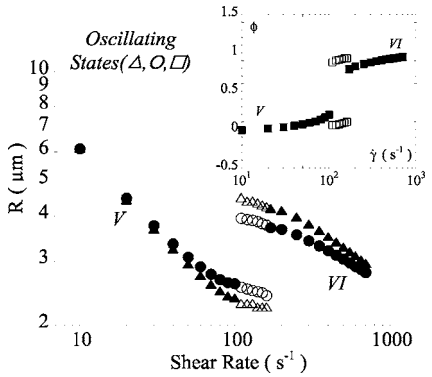

FIG. 22. Variation of the droplet size R (circles and triangles) with $\dot{\gamma}$ for the numerical simulations of the phenomenological model. Inset: shown is the evolution of the order parameter (squares) with the imposed shear rate (numerical simulations). Closed and open symbols stand respectively for the steady states and the oscillation regime. The different values of the numerical parameters are $\alpha=0.5$, $\tau_2=65$ s, and $k=3$ (●, ○) or 5 (▲, △, ■, □).

b. Numerical results. Our set of two coupled differential equations is numerically solved using MAPLE software. Figure 21 shows the variation of the steady state droplet size and order parameter for stress controlled experiments as a function of the applied stress.

In good agreement with our experimental observations: (i) two steady state branches separated by a discontinuous jump of the droplet size are obtained and (ii) no droplet size oscillations are observed. Now, if the shear rate is imposed, these two steady state branches are still observed. However, for intermediate shear rate values, the droplet size becomes a periodical function of time (see Fig. 22) as experimentally reported.

In Fig. 23, temporal variations of both the droplet size and the order parameter for different values of applied shear rates are shown. As evident, this model reproduces well droplet size oscillations (Fig. 23). It should be noted that these droplet size oscillations are coupled with oscillations of ϕ.

VII. CONCLUSION

By means of different rheophysics techniques, we have shown that the response of a two-phase fluid under flow can be extremely rich when the microstructure of one of the two coexisting phase exhibits strong nonlinear couplings with the flow. In particular, for the L_α/L_3 two-phase mixture presented herein, we have highlighted the existence under shear flow of several steady states, made of either monodisperse droplets (exhibiting or not a long range order) or elongated structures. We have shown that the transition between droplets and ESs is associated to a shear-induced phase inversion. As for monophasic complex fluids under flow, these steady states are separated by dynamic out of equilibrium transi-

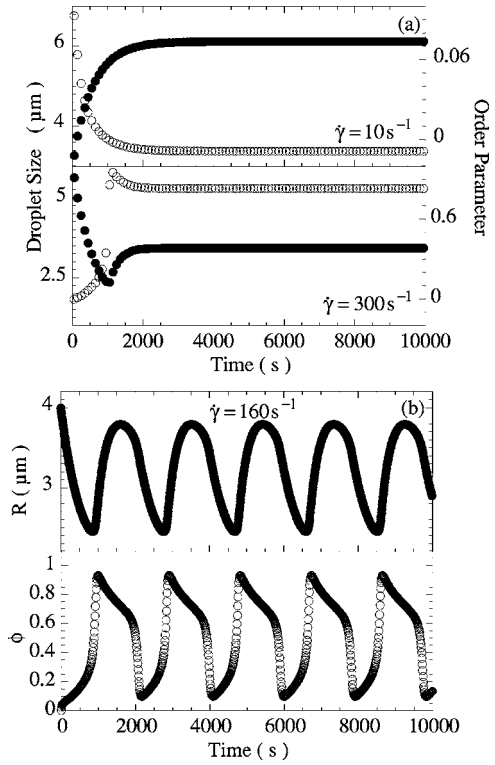

FIG. 23. Temporal variations of both the droplet size R (●) and the order parameter ϕ (○) for different values of $\dot{\gamma}$: (a) $\dot{\gamma}=10\ s^{-1}$ [the initial values are $R(t=0)=3\ \mu$m and $\phi(t=0)=0$] and $\dot{\gamma}=300\ s^{-1}$ with $R(t=0)=6\ \mu$m, and $\phi(t=0)=0$. (b) $\dot{\gamma}=160\ s^{-1}$, $R(t=0)=6\ \mu$m and $\phi(t=0)=0$. The values of the numerical parameters are, respectively, $k=3$, $\alpha=0.5$, and $\tau_2=65$ s.

tions. Depending on the nature of the imposed dynamic variable (stress or shear rate), structural bistability or shear banding can be observed. The originality of our work is to show that the dynamics of two-phase flows can be richer and lead to structural oscillatory states for which the droplet size becomes a periodical function of time. To account for this astonishing phenomenon, we propose a feedback scenario, based on water release from the droplets above a critical stress. Following this idea, a phenomenological model can be built using two coupled differential equations describing respectively the mechanical response of the droplet size under stress and the resulting osmotic transfer of water through the membranes. Despite the large apparent number of parameters required, it turns out that most of them (six out of nine) can be deduced from SALS and rheology measurements. Agreement between experimental observations and numerical simulations is excellent. Our present study therefore suggests that the droplet size may exhibit more complex dynamic behavior such as, for instance, chaos. Nevertheless, to get a chaotic behavior, one would either require spatial inhomogeneity (compatible with the transient shear banding observed during oscillations) or a third independent dynamical variable coupling with the droplet size and the water content. This third dynamical variable could be for instance the density of the pore defects in the lamellar phase controlling water permeation. Such density is certainly controlled by the osmotic pressure and therefore should depend on both temperature and stress. We hope that this open question will motivate theoretical works along such lines. Extensive studies as a function of surfactant composition, temperature, and salinity are now being performed in our group to try to bring experimental proof of this possible phenomenon. Another important point we wish to stress is the fact that droplet size oscillations seem embodied in the existence of a shear-induced change of surface tension between the two coexisting phases. That is why we strongly believe that such a phenomenon may be general and occur in other two-phase flows of complex fluids.

ACKNOWLEDGMENTS

It is a pleasure to thank L. Noirez for technical assistance in performing SANS experiments and P. Reinheimer and P. Sierro for their help with the commercial rheoscope (ThermoHaake).

[1] *Micelles, Membranes, Microemulsions and Monolayers*, edited by W. M. Gelbart, A. Ben-Shaul, and D. Roux (Springer-Verlag, New York, 1994).
[2] See, for instance, H. A. Stone, Annu. Rev. Fluid Mech. **26**, 65 (1994), and references therein.
[3] G. I. Taylor, Proc. R. Soc. London, Ser. A **146**, 501 (1934).
[4] T. Hashimoto, K. Matsuzaka, E. Moses, and A. Onuki, Phys. Rev. Lett. **74**, 126 (1995); Phys. Rev. E **56**, 6970 (1997); S. Saito and T. Hashimoto, J. Chem. Phys. **108**, 6963 (1998).
[5] K. Y. Min and W. I. Goldburg, Phys. Rev. Lett. **70**, 469 (1993); , **71**, 569 (1997); K. Asakawa and T. Hashimoto, J. Chem. Phys. **108**, 6963 (1998).
[6] G. Cristobal, J. Rouch, P. Panizza, and T. Narayanan, Phys. Rev. E **64**, 011505 (2001); see also P. Panizza L. Courbin, G. Cristobal, and J. Rouch, in *Recent Research Developments in Surface and Collids*, edited by A. Gayateri (Research Singpost, Kerala, 2004), and references therein.
[7] T. G. Mason and J. Bibette, Phys. Rev. Lett. **77**, 3481 (1996).
[8] A. Onuki, Europhys. Lett. **28**, 175 (1994); I. S. Miles and A. Zurek, Polym. Eng. Sci. **28**, 796 (1988).
[9] P. Nozieres and D. Quemada, Europhys. Lett. **2**, 129 (1986); V. Schmitt, C. M. Marques, and F. Lequeux, Phys. Rev. E **52**, 4009 (1995).
[10] R. W. Mair and P. T. Callaghan, Europhys. Lett. **36**, 719 (1996); M. M. Britton and P. T. Callaghan, Phys. Rev. Lett. **78**, 4930 (1997); S. Lerouge, J. P. Decruppe, and C. Humbert, *ibid.* **81**, 5457 (1998); J. P. Decruppe, S. Lerouge, and J. F. Berret, Phys. Rev. E **63**, 022501 (2001); J. K. G. Dhont, *ibid.* **60**, 4534 (1999); C. Y. David Lu, P. D. Olmsted, and R. C. Ball, Phys. Rev. Lett. **84**, 642 (2000); J. F. Berret and G. Porte, Phys. Rev. E **60**, 4268 (1998).
[11] P. Panizza, P. Archambault, and D. Roux, J. Phys. II **5**, 303

(1995); D. Bonn, J. Meunier, O. Greffier, A. Al-Kahwaji, and H. Kellay, Phys. Rev. E **58**, 2115 (1998); G. Cristobal, J. Rouch, A. Colin, and P. Panizza, *ibid.* **62**, 3871 (2000).

[12] R. Bandyopadhyay, G. Basappa, and A. K. Sood, Phys. Rev. Lett. **84**, 2022 (2000); W. M. Holmes, M. R. Lopez-Gonzales, and P. T. Callaghan, Europhys. Lett. **64**, 274 (2003); M. M. Britton and P. T. Callaghan, Eur. Phys. J. B **7**, 237 (1999).

[13] R. Bandyopadhyay and A. K. Sood, Europhys. Lett. **56**, 447 (2001); Y. T. Hu, P. Boltenhagen, and D. J. Pine, J. Rheol. **42**, 1185 (1998).

[14] A.-S. Wunenburger, A. Colin, J. Leng, A. Arnéodo, and D. Roux, Phys. Rev. Lett. **86**, 1374 (2001); J.-B. Salmon, A. Colin, and D. Roux, Phys. Rev. E **66**, 031505 (2002); C. Meyer, S. Asnacios, C. Bourgaux, and M. Kleman, Mol. Cryst. Liq. Cryst. Sci. Technol., Sect. A **332**, 531 (1999).

[15] P. Panizza, L. Courbin, G. Cristobal, J. Rouch, and T. Narayanan, Physica A **332**, 38 (2003).

[16] D. Lootens, H. Van Damme, and P. Hébraud, Phys. Rev. Lett. **90**, 178301 (2003).

[17] C. Pujolle-Robic and L. Noirez, Phys. Rev. E **68**, 061706 (2003).

[18] P. Fisher, Rheol. Acta **39**, 234 (2000).

[19] A. Aradian and M. E. Cates, Europhys. Lett. **70**, 397 (2005).

[20] S. M. Fielding and P. D. Olmsted, Phys. Rev. Lett. **92**, 084502 (2004).

[21] D. A. Head, A. Ajdari, and M. E. Cates, Phys. Rev. E **64**, 061509 (2001); Europhys. Lett. **57**, 120 (2001); M. E. Cates, D. A. Head, and A. Ajdari, Phys. Rev. E **66**, 025202(R) (2002).

[22] M. Grosso, S. Crescitelli, E. Somma, J. Vermant, P. Moldenaers, and P. L. Maffettone, Phys. Rev. Lett. **90**, 098304 (2003); M. Grosso, R. Keunings, S. Crescitelli, and P. L. Maffettone, *ibid.* **86**, 3184 (2001).

[23] L. Courbin, P. Panizza, and J.-B. Salmon, Phys. Rev. Lett. **92**, 018305 (2004).

[24] O. Gosh and C. A. Miller, J. Phys. Chem. **91**, 4528 (1987).

[25] E. Freyssingeas, F. Nallet, and D. Roux, Langmuir **12**, 6028 (1996).

[26] http://www.thermo.com

[27] C. Hashimoto, G. Cristobal, A. Nicolas, P. Panizza, J. Rouch, and H. Ushiki, Meas. Sci. Technol. **12**, 514 (2001).

[28] C. Blanc, Phys. Rev. E **64**, 011702 (2001); O. Lavrenvovich, C. Quillet, and M. Kleman, J. Phys. Chem. B **101**, 420 (1997).

[29] T. Hashimoto, T. Takebe, and S. Suehiro, J. Chem. Phys. **88**, 5874 (1988).

[30] L. Courbin, G. Cristobal, J. Rouch, and P. Panizza, Europhys. Lett. **55**, 880 (2001); L. Courbin and P. Panizza, Phys. Rev. E **69**, 021504 (2004).

[31] P. D. Olmsted, Europhys. Lett. **48**, 339 (1999).

[32] O. Diat, D. Roux and F. Nallet, Phys. Rev. E **51**, 3296 (1995); P. Sierro and D. Roux, Phys. Rev. Lett. **78**, 1496 (1997).

[33] L. Courbin, W. Engl, and P. Panizza, Phys. Rev. E **69**, 061508 (2004).